# S262: Setting up a Radio-Astronomical Receiver/ Setting up a Radio Interferometer

A7

Jacob Cardinal Tremblay, Pranav Limaye

November 15, 2022

# Contents

# 1 Introduction

The aim of this lab is to understand the working principle behind a radio astronomical receiver, more specifically the superheterodyne receiver system and to understand how a radio interferometer works. The lab is subdivided in two parts. The first part deals with studying different properties of the components of a superheterodyne receiver. After studying the individual components, the receiver is used to catch signals from a signal generator generating a spectral line at a fixed frequency which will allow to study the response of the receiver system. The second part of the experiment involves working with a twin radio interferometer. The setup is used to observe the Sun and make an interference image of it and further deduce some results from this output.

# 2 Basics of Radio Interferometry

This introduction to the world of radio astronomy is our very own summary and interpretation of the topics mentioned in the 2022 lab manual by Jürgen Kerp, along with other sources which are cited. Please view the information in this report as a concise version of the material, focused around the specific tasks performed. For a full understanding, please seek information from our cited sources.

## 2.1 Setting Up a Radio-Astronomical Receiver

In this section, several important terms for the experiment are defined. These are terms which have been indicated in **bold** in the lab script [24] and are once again bolded in this text before they are defined.

Starting with the absolute basics, an **electrical signal** is either a voltage or current which can relay information in a circuit. This electrical signal will contain an amplitude, a time period and a frequency (number of cycles per second) [22]. In the case of this lab, electromagnetic signals collected by a radio telescope will be converted to an electrical signal.

Huge amplifications of such signals are necessary which is why a superheterodyne receiver is generally used. This experiment will make use of such a receiver and allow the students to familiarize themselves with the active and passive components of a receiver. A working receiver will be set set with **down-conversion** of the high-frequency signal to an **intermediate frequency**.

This down-conversion is when a signal is converted to a lower frequency at a lower sampling rate to simplify further radio stages. This process should preserve all the information of the original signal [7]. An intermediate frequency (IF) is a frequency between the baseband frequency and the carrier frequency. Using an IF allows the design of a receiver where the circuitry can be designed for a single unchanging frequency band [23].

This signal is then detected by a **backend**, where the alternating signals are transformed into a form useful for science. The backend refers to the instruments which are not directly attached to the telescope. This term can be used for many parts of an instrument, for example the correlator in a radio interferometer. The frontend will perform operations which make the signal easier to transmit, and the backend will carry the rest of the processing in a more protected environment [13].

In the case of continuum observations, the backend provides a power signal over a **bandwidth**, which is a continuous band of frequencies, along with polarization parameters.

There is also a spectroscopy portion to this lab, where the frequency dependence of the signal is analysed with high **spectral resolution**. This spectral resolution is defined as the ability of a sensor to define fine wavelength intervals [5]. Therefore in this context is means that the frequency spectrum will have fine intervals that will allow for a detailed investigation of the frequency spectrum.

In the experiment itself, a backend which delivers a signal proportional to the power will be used as well as a spectrum analyzer to study frequency dependence.

Amplification of the signal is done using the superheterodyne method which is a step-wise amplification of the signal at multiple frequencies. The original signal is converted to a lower frequency with the use of a mixer. The general idea is to use a **superheterodyne receiver**. This is a type of radio receiver which converts received a radio signal into an intermediate frequency (IF) through the use of a mixer. These IF signals can then be processed more easily than the original ones [24].

Each of the receiver component can be characterized by a **gain** G. Gain is an important parameter in radio astronomy as it is a performance parameter which combined the antenna's directivity along with the radiation efficiency. It is essentially the maximum radiation intensity produced by the antenna compared to that given by a lossless isotropic radiator supplied with the same level of power [20]. It has units of dB or dBm. Passive components will have a G ¡ 1 and the total amplification of a receiver is given by the product of all the individual gains (sum of the gains in dB).

Another important parameter of a receiver is the **Noise Temperature**. This value is what would be measured if the receiver did not have any input signal which will therefore define the detection limit [24]. This value can be calculated for every component however the first component will be the most important as further components will have progressively smaller contributions. In practice, it is best to determine the receiver using a hot-cold calibration where a resistor at room temperature is compared to one cooled in liquid nitrogen. This process will be further explained in the section where such a calibration takes place. Finally, the limiting sensitivity is not only given by the noise temperature, but also by variations in the gain and other instabilities.

## 2.2 Understanding a Radio Interferometer

Radio Telescopes are capable of observing astronomical sources from the ground as radio waves are not blocked by the atmosphere. However, radio astronomy also has a finite window for getting the optimum results. For example, high frequency radio observations suffer from absorption in the atmosphere due to the water vapour content of this layer. On the other hand, low frequency radiation gets scatter by the ionosphere producing signal fluctuations known as "scintillations'. Above a certain wavelength, the radio waves get reflected back from the atmosphere. However, for wavelengths between 1-20cm, the atmospheric attenuation is not very crucial and using robust calibration algorithms can help take care of the the further signal processing [24].

An antenna is the most basic component of a radio telescope and its most critical property is the **sensitivity**. It depends on the aperture efficiency of the telescope and the coupling of the antenna with the incoming radio waves. Sensitivity of a radio telescope gives a threshold for detecting astronomical signals with the instrument. As an example, for a continuum observation with the Meerkat array in the L-band, the sensitivity is 3.1 $\mu$Jy/beam [Refer :Meerkat Sensitivity Calculator]. This means that the array can observe sources as faint as 3.1 $\mu$Jy which is really unprecedented capability that has been achieved today. The sensitivity also depends on the system temperature and inversely on the observing bandwidth and integration. This relation is expressed as the famous **'radiometer equation'** which is given as :

$$\Delta T = \frac{T_{sys}}{\sqrt{\Delta\nu.\tau}} \tag{1}$$

where for a radio interferometer, $T_{sys}$ is the system temperature, $\Delta\nu$ is the correlator bandwidth and $\tau$ is the integration time.

Radio Telescopes have can be built in various different structural aspects. Low frequency radio telescopes are often an array of dipole antennas like the LOFAR while high frequency observations need parabolic dish telescopes like the Green Bank 100m Telescope in the US. Thus, **wavelength of operation** has a crucial role to play while designing radio telescopes. For centimeter wavalenghts, the surface precision is not a concern but for millimeter wavelengths, the parabolic dishes should have high precision,i.e, very little surface variations. Hence, we see that high frequency dishes have a smaller diameter as it is easier to achieve the required amount of precision on small surfaces.

The **angular resolution** of a radio telescope is its property to resolve sources on the **smallest angular scales** which depends on the wavelength of observation and the diameter of the telescope for a single dish telescope given as:

$$\theta = 1.22\frac{\lambda}{D} \tag{2}$$

In case of a radio interferometer, the resolution depends on the largest spatial separation between any two dishes in the array also known as the **baseline B** and is given by:

$$\theta = 1.22\frac{\lambda}{B} \tag{3}$$

Quantitatively, it is the **diffraction limit** of a interferometer which gives the smallest recoverable angular scales. Larger the baselines give closely spaced fringes and hence better angular resolution. On the other hand, the antennas with the least separation or the shortest baseline give the **maximum recoverable angular scale** in the sky. It is very important in radio interferometry to recover large scales but also give a good resolution. Therefore, observations are often carried out where the array can be subdivided such that an array selection with the largest baseline gives the resolution while the other half of the array consists of closely spaced antennas to give a better sense of the largest scale of the target.

Any radio telescope records the **brightness distribution** of the source which is defined as the power spectrum it generates as from the electric field distribution at the antenna aperture. In an interferometer, a pair of two radio telescopes produces a visibility which is a correlation of the brightness distribution recorded at the two radio telescopes. Technically speaking, the two dishes generate a voltage which are cross-correlated giving the visibility. Mathematically, visibility is a fourier transform of the far-field onto the aperture. Hence, getting visibilities is producing fourier components using complext fourier transform algorithms. One such algorithm is the **Fast Fourier Transform** which calculates a discrete fourier transform since the

signal is digital, but with reduced computational effort.
The visibilities that we get are discrete points on the spatial scale. The way to increase these points is to add more antennas to the interferometer and hence increase the correlations and the visibility. However, another clever method to fill up the so called uv-plane in interferometry is doing aperture synthesis which uses the earth's rotation to fill-up the voids between the visibilities and produce radio images. Once the raw data is in, making a radio image from it is another difficult task. Algorithms like CLEAN are used to improve the image quality and self-calibration is performed by dedicated softwares like CASA.

## 2.3 Equatorial Coordinate System

There have been used several coordinate systems used in Astronomy to specify the location of celestial sources. Briefly, the coordinate systems can be relatively specified into three systems. The topocentric system considers the observers location as the origin, the geocentric system considers the Earth's center as the origin while the heliocentric system considers the Sun's center as the origin. The most commonly used coordinate system used today is the equatorial coordinate system which is geocentric. A representation of this system can be seen in Fig. 1.

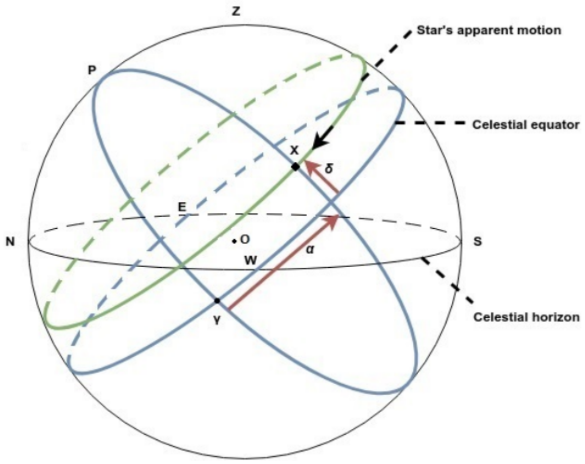

Figure 1: The Equatorial Coordinate System (credits: [24])

In the above coordinate system, let $\phi$ be the latitude of the observer. Then the **zenith** Z is the point directly overhead the observer which forms the pole of the horizon. Earth is the center of this system with an imaginary celestial sphere arounf it. The celestial equator is an imaginary line extending from the Earth's equator onto the celestial sphere and the point P is the pole of the celestial equator. The **Right Ascension** and **Declination** are analogous to the longitude and latitude. The Right Ascension $\alpha$] sweeps from the right to left and is usually measured in units of hours, minutes and seconds. The Declination $\delta$ is the elevation angle in degrees measured from the equator, with 90° being the North Pole and -90° is the South Pole. A **meridian** is a great semicircle passing through the celestial pole. The angle between the meridian of the celestial object and observer is called the **Hour Angle**. It is measured westwards from the observer's meridian tracing from 0h to 24h.

## 2.4 Radio emission from the Sun

Sun is the brightest radio source in the sky and hence, it is also an unwanted white noise which can deteriorate observations of other faint radio sources. It is a **thermal source** of radiation meaning its a blackbody following the Planck's Law. It emits most of its radio radiation thermally at high frequencies but also shows a fraction of synchrotron emission at the lower frequencies.

## 2.5 Questions for Part II (Interferometry)

**Exercise 2.1 Which property of the telescope can affect angular resolution and image quality?**
As it can be seen from Eqn. 2, the angular resolution is inversely dependant on the telescope diameter. Therefore, increasing the dish diameter can improve the resolution. However, if the angular resolution were to be fixed, the resolution will get poorer for low frequency observations while it will be bad for high frequency observations if the dish surface variations are high. Thus, these effects on the angular resolution have a direct impact on the image quality.

**Exercise 2.2 What is the difference between the wavelengths of operation at radio telescopes with small and big parabolic surfaces?**
High operating frequencies require less surface accuracy compared to low frequency observations. Moreover, from the equation for angular resolution it can be seen that, smaller dishes are more suited for high frequency observations while we need big dishes for low frequency observations.

**Exercise 2.3 How can you prove the equality of the altitude of the north celestial pole and the latitude of the observer?**

Observer Latitude: The observer's latitude is the angle that the celestial equator makes with its zenith.
Altitude of North Celestial Pole : Angle of the north celestial pole above the observer's horizon.
This problem can be better solved using a visual representation as shown in Fig. 2.

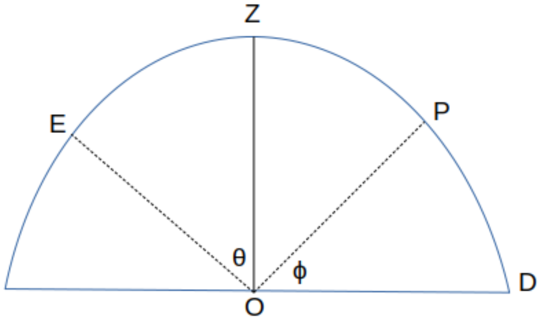

Figure 2: Representation of coordinate system as seen by the observer

Let Z be the zenith of the observer O, P be the celestial pole and E the celestial equator respectively. Therefore, by definition we have:
$\angle$ EOZ = $\theta$ : Observer's Latitude
$\angle$ POD = $\phi$ : Altitude of North Celestial Pole
The angle between the celestial equator and north celestial pole is, $\angle$ EOP = 90°. Hence, we can carry out a simple geometry exercise as follows:
$\angle$ ZOP = 90 - $\theta$
which implies,
$\angle$ POD = 90 - (90-$\theta$)
Therefore, we get $\theta = \phi$, hence the proof that the altitude of the north celestial pole is equal to the latitude of the observer.

**Exercise 2.4 How many full moons can be laid side-by-side within Polaris' circular path about the north celestial pole?**

The pole star is at a distance of about 60' from the north celestial pole giving the diameter of its circular path as 120'. The angular size of the moon is about 30'. Therefore, we can fit 120'/30', i.e, four full moons within the Polaris' circular path around the north celestial pole.

**Exercise 2.5 Solar atmosphere has three main layers: the photosphere, the chromosphere and the corona. What kind of emission does each layer emit? Which layer(s) does(do) emit in radio wavelengths?**

1) Photosphere: The photosphere forms the surface from which we get visible light. The temperature of this layer varies between 4500K-6000K [reference]. There is no radio emission seen in this layer as it is dominated by high energy thermal emission.

2) Chromosphere: This layer lies between the photosphere and the corona. This layer is well known for H$\alpha$ emission lines and UV radiation. The layer also exhibits radiation at millimeter wavelengths into the radio through thermal as well as non-thermal processes to some extent [12].

3) Corona: This is the outermost layer of the Sun which contains ionized plasma and has a temperature reaching upto $\sim$ 2.3 million kelvin [reference]. It emits in UV, X-ray and radio. The radio emission is dominated by thermal and non-thermal processes [12].

**Exercise 2.6 What is the origin of the radio emission of the corona**

The radio emission in the solar corona is dominated by thermal and non-thermal processes. There are a total four emission mechanisms that dominate this emission : free-free emission, gyromagnetic emission, plasma emission and electron-cyclotron emission [18].

**Exercise 2.7 Plot the flux density vs. frequency for three different sources (e.g. 1000, 4000, 8000) and place the solar emission profile on it. Does the Sun have a perfect black body radiation?**

A Blackbody emission follows the Planck's Law which is given as :

$$B(\nu, T) = \frac{2h\nu^3}{c^2}\frac{1}{e^{\frac{h\nu}{k_B T}} - 1} \tag{4}$$

Using this relation, we plotted the energy density B($\nu$,T) as a function of frequency for different temperatures and for the temperature of the Sun ($T_sun = 5800$K). The results have been shown in Fig. 3.

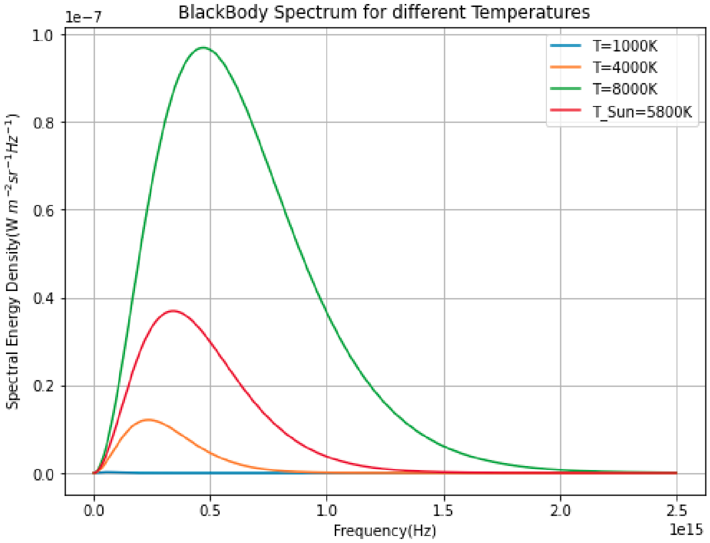

Figure 3: Energy Density Vs Frequency for a Planck Spectrum

From this figure, it can be seen that the Sun follows the Planck's law very well and can be approximated to be a very good blackbody. However, there can be deviations from this spectrum due to the temperature variations in the Sun.

**Exercise 2.8 What is the difference between the radio emission of the active Sun and the quiet Sun? Locate both in the plot.** The radio emission shows significant variation during the active and quiet phases. The Sun has a 11year solar cycle over which its magnetic field is completely flipped [reference]. The start and end of this cycle shows minimum solar activity and is termed as the Quiet Sun. During this time, a very few sunspots are visible on the Sun. On the other hand, the period when the solar activity peaks is the Active Sun. The difference between the active and quite Sun radio emission can be clearly seen in its spectrum as shown in Fig. 4. For comparison, this plot shows the spectrum during these two phases at a frequency of 2.6GHz and we can see that there's a difference of an order of magnitude in the flux density between the two phases. The increased amount of emission during the active phase can be attributed to hugh number of solar flares produced during the period.

**Exercise 2.9 In which case can we see the Sun bigger in size? Observing the photosphere or the corona?**

The Sun will appear bigger when observing the corona as compared to observing the photosphere. The photosphere is a much thin layer and is confined to optical emission whereas the corona stretches out millions of kilometers from the solar surface and is dominated by radio emission. Hence, the radio Sun is bigger than the optical Sun. This can be also proved during a total eclipse where, the dip produced in the flux will stay for a longer time during radio observations as compared to optical observations. This dip in the flux will start before the optical eclipse starts and will end at a delayed time after the visible eclipse is over.

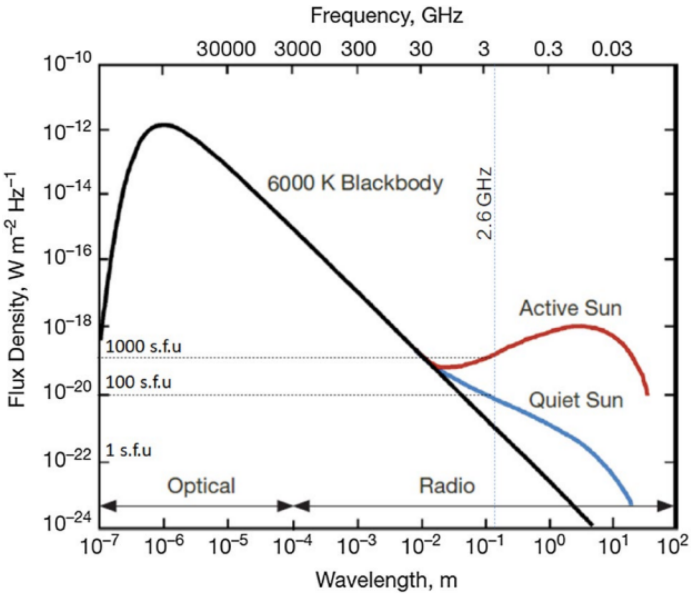

Figure 4: Radio spectrum of the Sun during the active and quiet periods (credits: [19])

# 3 Setting up a Radio Astronomical Receiver

## 3.1 Measuring Individual Components

Before heading into the exercises, it is important to define some of the individual components with which we will be working. Definitions are based from the information in the lab manual [24].

An **amplifier** is a device which amplifies an input power signal. Using an electronic power supply, it then increases the amplitude, and the gain of such a device will then provide information about the amount of amplification which is more than one.

A **filter** is a device used to eliminated unwanted frequencies or bands of a signal.

A **mixer** is a device which can combine multiple radio signals into a single output signal.

### 3.1.1 Exercise 1.1

The first exercise was to determine the gain of three amplifiers (`HF-V1`, `HF-V2`, `ZF-VI`), however during the experiment only two high frequency amplifiers were available (`HF-V1` and `HF-V2`) and therefore these were the only amplifiers used in the experiment. The properties of these amplifiers can be found in Tab. 1. The properties of amplifier `HF-V1` were first measured and the properties of `HF-V2` were measured after. In order to measure these properties, the first step was to connect the signal generator to the input of the amplifier and then to the power meter to the output. The amplifier was connected to a power supply (of ±15 V) and the input frequency was set to 2.3 GHz. For `HF-V1`, the amplitude (input power) was set to 20 dBm and was decreased by steps of 2 dBm until -30 dBm. The same was done for `HF-V2`, however here the amplitude was decreased until -40 dBm instead of -30 dBm so that the behaviour of the amplifier was better resolved. An uncertainty for the values of amplitude of ±0.10 dBm was then applied to each measurement in order to account for possible human error on the reading. An important thing to note is that in order to acquire a reading on the power meter, it was important to gradually decrease the power meter range accordingly. The output power would then be the result of the range and the reading added together. The amplifiers were operated in linear regime in order to obtain a pure amplification.

| Amplifier | Gain [dB] | Bandwidth [GHz] | 1 dB-Compression Point [dBm] | Temperature [K] | Function |
|---|---|---|---|---|---|
| `HF-V1` | 11.508 ± 0.159 | ≈ 2-3 | 6 | 150 | HF-pre-amplifier |
| `HF-V2` | 28.479 ± 0.634 | 2-4 | 13 | 400 | HF-amplifier |

Table 1: Parameters of the two amplifiers used during this experiment. The only measured values are the gain, the other values were provided by the lab manual [24]. No uncertainties were provided on the numbers given by the lab manual, which is why there are only uncertainties on the measured gain values.

In order to acquire the values for gain, the input power had to be plotted against the output power. The `Python` programming language [27] along with the `Matplotlib` package [3] was used to plot these values and is also used throughout the report to make all other plots and non-trivial calculations. This resulted in Fig. 5 and Fig. 6, where a linear regression was then made in the linear regime using the `Numpy.polyfit Python` package [9]. For `HF-V1` this meant selecting points with indexes 14 to 22, whereas for `HF-V2` points with indexes of 19 to 31 were selected. This linear regression was then performed (using the equation of a straight line: $y = mx + b$) which resulted in a value for slope ($m$) and y-intercept ($b$). The values for the fit parameters are the respective slope and y-intercept of each amplifier. The value for the y-intercept is our value for the gain and is shown in Tab. 1.
Values for the slope were calculated to be $0.727 \pm 0.010$ for `HF-V1` and $0.948 \pm 0.021$ for `HF-V2`. For an ideal gain, where we are completely in the linear regime, the slope would be of exactly 1. One can therefore see that `HF-V1` is relatively off however `HF-V2` is quite close to the ideal gain.

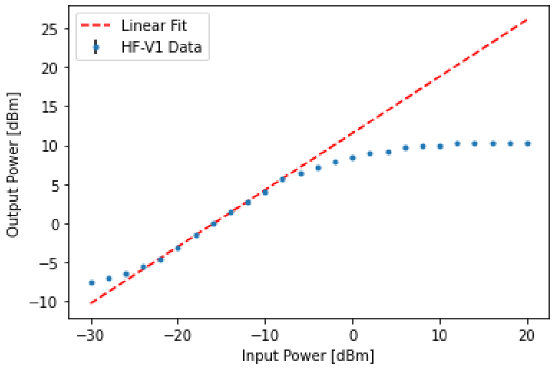

Figure 5: Output power vs. input power for `HF-V1` with a linear fit applied to the linear regime. Uncertainties of ±0.1 dBm on all points are present, however they are too small to be visible.

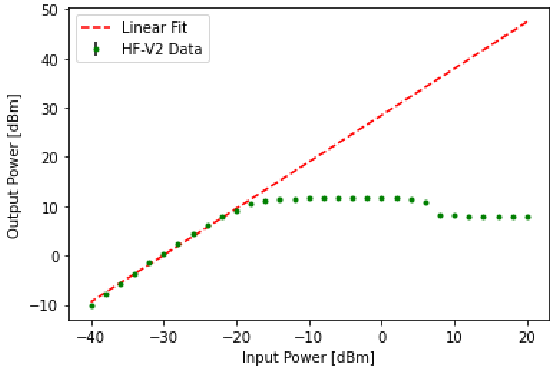

Figure 6: Output power vs. input power for `HF-V2` with a linear fit applied to the linear regime. Uncertainties of ±0.1 dBm on all points are present, however they are too small to be visible.

### 3.1.2 Exercise 1.2

The second task for this part of the lab was to measure the input and output power of the filter at different frequencies around the central frequency. This is done with the overall goal of investigating the most important parameters of filters, namely, central frequency, bandwidth, adjacent-band rejection and insertion loss. In order to do this, a similar setup to the previous exercise was set, however this time the amplifier was replaced with the appropriate filter. For this experiment, two different filters were provided. Filter `HF-F1` was the high-frequency filter had a theoretical central frequency of 2.3 GHz with an uncertainty of ±25 MHz. The other filter, `ZF-F1`, was the low-frequency filter and had a theoretical central frequency of 150 MHz ±25 MHz. The `HF-F1` filter was examined first using a constant amplitude of 5 dBm. The frequency range started from 2.25 GHz as this was the minimum frequency where a signal was detected on the power meter. The frequency was then increased by 0.01 GHz until 2.45 GHz and the corresponding reading and range was recorded from the power meter for each frequency. An uncertainty of ±0.1 dBm was

applied to each recorded value in order to account for human error in reading the value on the power meter.
A similar process was then conductor for filter `ZF-F1`, however this time the frequency range first detected a signal around 100 MHz so the frequency range was started at 100 MHz and stopped at 200 MHz. The frequency was increased by steps of 5 MHz and the corresponding reading and range was recorded from the power meter for each frequency. Once again an uncertainty of ± 0.1 dBm was applied to each recorded value in order to account for human error in reading the value on the power meter. It is also important to note that in both parts of this exercise, any loose connections could have increased the error on the readings obtained however as no evidence for such was observed, this was considered to be insignificant. A more thorough analysis (outside of the scope of this report) could calculate the affect of such loose connections and the probability that it would significantly affect the measured uncertainty.

From the measured values, the output frequencies were calculated which once plotted against frequency resulted in Fig. 7 for `HF-F1` and Fig. 8 for `ZF-F1`. Since the resolution of our spectrum is not extremely fine, an ideal solution would have been to fit a bandpass filter to the current data to determine the shape of the full frequency response. This could in turn be used to determine the -3 dBm cut-off by subtracting 3 dBm from the filter value. However, creating such fits with `Python` packages such as `scipy.signal.butter` turns out to be not at all trivial and therefore a more simple approach was used. The approach used was to take an average of the 7 data points with the largest output power and subtract 3 dBm from this average power. This resulted in a -3 dBm cut-off value of $-0.671 \pm 0.037$ dBm, which corresponds to half the drop of maximum power in Watts.

For the measured values using `ZF-F1`, one can see from Fig. 8 that the full spectrum was recorded once again. Once again here, rather than fitting a bandpass filter, it was decided to take an average of the 9 data points with the largest output power and subtract 3 dBm from this average power. The result was a -3 dBm cut-off value

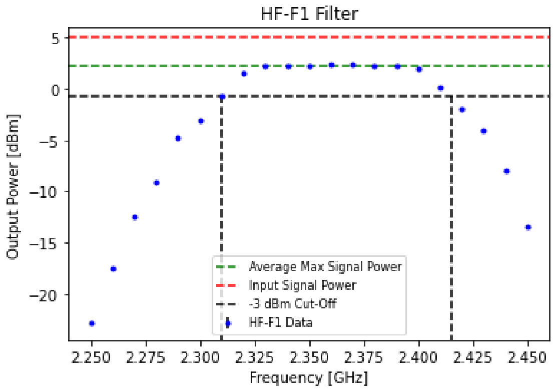

Figure 7: Frequency response for the `HF-F1` filter. Input signal power was of 5 dBm, the average of the maximum signal power was of 2.329 ± 0.037, and 3 dBm below the maximum output power was of -0.671 ± 0.037. Uncertainties of ±0.1 dBm on all points are present, however they are too small to be visible.

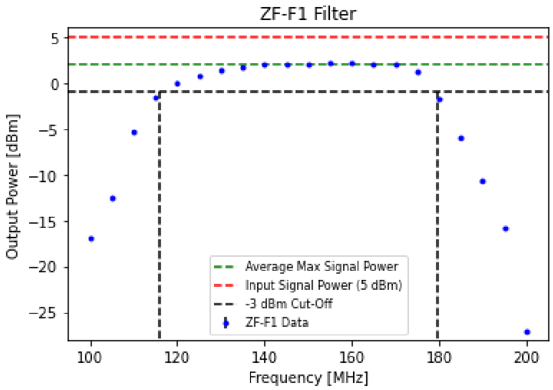

Figure 8: Frequency response for the `HF-F1` filter. Input signal power was of 5 dBm, the average of the maximum signal power was of 2.028 ± 0.037, and 3 dBm below the maximum output power was of -0.971 ± 0.037. Uncertainties of ±0.1 dBm on all points are present, however they are too small to be visible.

of $-0.971 \pm 0.037$ dBm which once again corresponds to half the drop of maximum power in Watts.

In both filters, the top 7 highest values of power were chosen to be used as the average maximum power. However this choice was completely arbitrary and the points were simply chosen because they were the highest values in a row which did not vary by more than 0.1 dBm. A more scientific justification could perhaps have been made, especially by using a bandpass filter fit, however in the case of this report it was justified that our method would produce a accurate enough results. In further work, a better justification for which points to use as the average of the maximum power could be made.
As there was no calibration steps for the instruments used in the lab, it is also possible that improper calibration has affected the results. Perhaps it would be important to perform calibrations in the future in order to rule out any systematic uncertainties.

The two values for the average maximum power appear consistent with values one would expect. Since for any RF device, the signal will have undergone some attenuation, the output power should be lower than the input power. This loss can then be measured by the insertion loss which is the ratio of the output signal to the input signal [1] and is calculated according to,

$$I.L. = 10\ \log_{10}\left[\frac{P_{\text{out}}}{P_{\text{in}}}\right]. \tag{5}$$

The insertion loss values for each filter are shown in Tab. 2. These values should always have a negative result (hence the “loss” term) as long as the output power is smaller than the input power. However, when expressing insertion loss in practice, it is common place to use the absolute value of the obtained negative result [16], which is why the values determined in Tab. 2 are positive.
Typically, the adjacent-band rejection is calculated as the frequency where the signal drops below the maximum signal by 60 dBm [26]. However in both of the filters, the powers are not probed to such low and high frequencies, and such low powers were not even detected by the power meter. Therefore rather than use the value

of 60 dBm, the lowest power values of the frequency spectrum shape were chosen, which means that the adjacent-band rejection will essentially be the entire frequency bandwidth. The lowest frequency and the highest frequency were then estimated from the shape of the frequency spectrum, and the difference gave the adjacent-band rejection. This was then calculated for both filters and displayed in Tab 2. As the upper and lower frequencies are visual approximations of the actual bandpass filter fit shape, an uncertainty of ±10 MHz was applied to the upper and lower frequency values. Although our values are good approximations, in further studies, it would be important to acquire more sensitive instruments, which can measure powers of 60 dBm below the maximum in order to determine a proper value of adjacent-band rejection.

The bandwidth of the filters correspond to the edges of the -3 dBm cut-off seen in Fig. 7 and Fig. 8. In other words it includes the frequencies where the output power is lower than maximum output power by 3 dBm. The bandwidth values for both filters are given in Tab. 2, because a bandpass filter was not applied, these values were mostly decided as a visual approximation, therefore an uncertainty of ±10 MHz was applied to each measured frequency.

| Filter | Center Frequency | Maximum Output Power [dBm] | Insertion Loss [dBm] | Adjacent-band Rejection [MHz] | Bandwidth [MHz] |
|---|---|---|---|---|---|
| `HF-V1` | 2.3 ± 0.025 GHz | 2.329 ± 0.037 | 3.319 ± 0.069 | 222 ± 14.1 | 105 ± 14.1 |
| `HF-V2` | 150 ± 25 MHz | 2.028 ± 0.037 | 3.918 ± 0.079 | 92 ± 14.1 | 63.5 ± 14.1 |

Table 2: Parameters of the two amplifiers used during this experiment. The only measured values are the gain, the other values were provided by the lab manual [24]. No uncertainties were provided on the numbers given by the lab manual, which is why there are only uncertainties on the measured gain values.

### 3.1.3 Exercise 1.3

In this exercise the the bandpass of the HF-F1 filter was supposed to be displayed on the oscilloscope and the central frequency of the filter was supposed to be varied. Unfortunately, since the oscilloscope was not accurate enough, the lab tutor instructed us not to carry out this exercise. Therefore it will be skipped during this report.

### 3.1.4 Exercise 1.4

In this exercise, a mixer was used along with an RF signal and a local-oscillator (LO) in order to verify that the output power of the mixer depends linearly on the RF signal. The mixer inputs were connected to the RF signal and the LO and the output was connected to the power meter. The RF signal was set to 2.3 GHz with an amplitude of 0 dBm and the LO was set in continuous wave mode and tuned to 2.45 GHz with an amplitude of 12 dBm. The input power was then started at -7 dBm and increased by steps of 1 dBm all the way to 15 dBm. The reading and range were both recorded, and once added together resulted in a value for the output power. An uncertainty of ±0.1 dBm was applied to each recorded value in order to account for human error in reading the value on the power meter.

The input power was then plotted against the output power which resulted in Fig. 9. A first glance at the points shows a clear non-linear behaviour at the edges however, there appears to be linear behaviour near the center. Therefore a linear fit (of the form $y = mx + b$) was calculated for both the entire set of data points and points 3 to 14 (counting from left to right) as those points appeared to show the most linear behaviour. The results of these fits can be found in Tab. 3. Although typically it is best to use only the raw data, selected data points could have been justified in this situation as there might be systematics which play a role at the lower and higher input powers which cause the behaviour to no longer be linear. This is specifically known at higher powers, such as what was shown in exercise 1.1, and therefore it is possible that similar behaviour was seen here. Therefore calculations were performed on both the entire data and selected data in order to cover both the possibilities that all the data is valid, or that some of the data is bad.

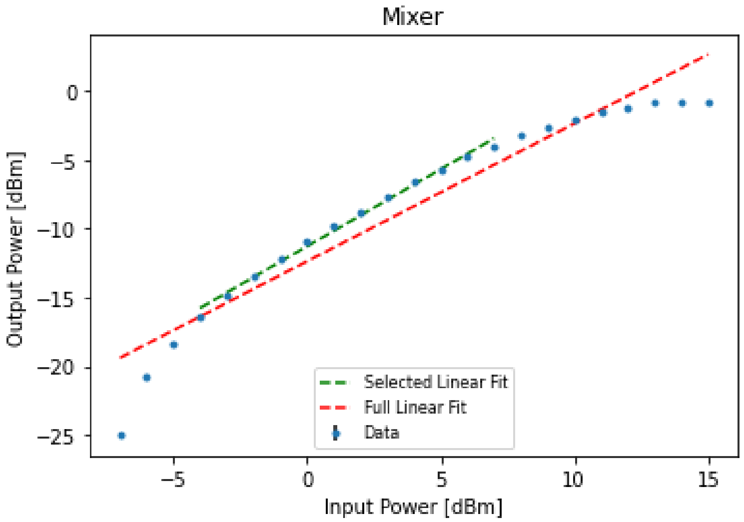

Figure 9: Output power as a function of input power for the mixer. Uncertainties of ±0.1 dBm on all points are present, however they are too small to be visible.

The conversion loss could then be calculated in dB by using the ratio of the RF input power to the IF single-sideband output power [6]. However, as we are working in dBm, the conversion loss is equivalent to the difference between the RF input power and the IF output power [8]. The result could then be acquired by looking at Fig. 9 and identifying where the output power starts to saturate. The absolute value for the two values of conversion loss were then included in Tab. 3, taking into account that the input power was 0 dBm.

| Fit | Slope [ ] | y-Intercept [dBm] | Conversion Loss [dBm] |
|---|---|---|---|
| Entire Fit | 1.001 ± 0.062 | -12.381 ± 0.486 | -1.2 ± 0.1 |
| Selected Fit | 1.121 ± 0.030 | -11.289 ± 0.114 | -3.2 ± 0.1 |

Table 3: Fit parameters of the linear fits of input power vs output power using the mixer as well as the calculated results for 1-dBm compression point and conversion loss. The entire fit is the fit applied to all data points whereas the selected fit is the fit applied to only the 12 points which show the most linear behaviour.

It is important to note that for this exercise, the results obtained from Fig. 9 needs to be taken with scrutiny. The behaviour observed was much less linear than what one would expect, and therefore there could be some systematic error which was not accounted for during this part of the lab. The values for the fit however still seem reasonable, and therefore the end result for the conversion loss should still be accurate, however the actual uncertainty most probably should be higher than the measured uncertainty on this value.

## 3.2 Measurements with a Complete Receiver

### 3.2.1 Exercise 1.5

In this part of the lab, we move from our simplified setup, to using that actual superheterodyne receiver. This receiver was constructed using the same types of components as in the previous exercises and comes completely pre-assembled so no parts needed to be changed. Calibration of the receiver was done using two well defined input powers. The input noise signal was provided by a matched 50 Ω resister (Load) and was first kept at room temperate. After the first measurements, at room temperature the laod was then cooled by liquid nitrogen at a temperature of 77 K.

The receiver was then connected to the signal generator and a frequency of 1.45 GHz was selected and an input power of 0 dBm was set. The hot-cold calibration measurements were then recorded on a PC connected to the receiver using the `Gqrx SDR` software [21]. This was first done by starting the recording at room temperature for a 30 seconds and then dipping the resistor into the liquid nitrogen. The recording continued until 60 seconds after the bubbling stopped and the data was saved. The provided `hotcold-power.py` script was then run on the raw data, which output the average power of each scan on the screen and in the end produce a usable text file.

The receiver temperature was then determined in two ways. The first way was to determine the temperature using Eq. 6.

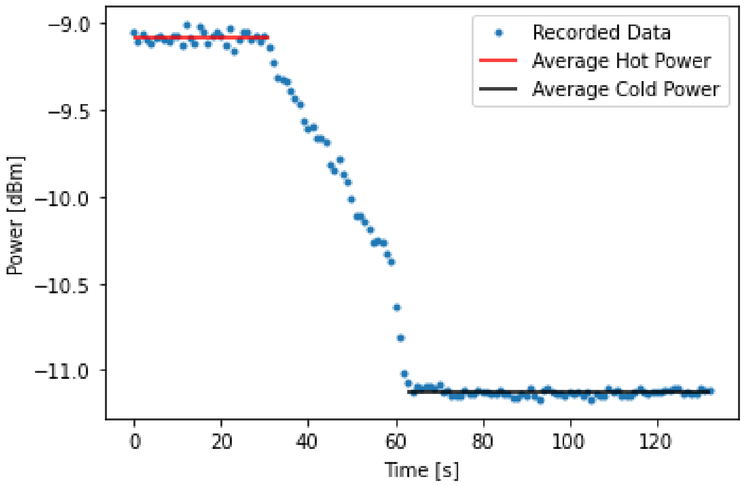

Figure 10: Output power vs. time for the hot-cold calibration as recorded by the `Gqrx SDR` software. The mean values of the hot power and cold power are also displayed.

$$T_{\text{rec, 1}} = P_{\text{cold}} \frac{T_{\text{hot}} - T_{\text{cold}}}{P_{\text{hot}} - P_{\text{cold}}} - T_{\text{cold}} \tag{6}$$

The room temperature was taken as $21.5 \pm 0.2$ °C and then converted to Kelvin. The temperature of the liquid nitrogen was known to be of 77 K, however since it was interacting with the environment and was not in a closed system, an uncertainty of $\pm 1$ K was assumed on $T_{\text{cold}}$. The values of output and input power were then converted to mili-Watt before calculating $T_{\text{rec, 1}}$. $P_{\text{hot}}$ was calculated by taking the average of the output powers at room temperature, whereas $P_{\text{cold}}$ was calculated by taking the average of the output powers after the system reached equilibrium. The calculations then resulted in values of $P_{\text{hot}} = 0.124 \pm 0.065$ mW and $P_{\text{cold}} = 0.077 \pm 0.040$ mW, where the uncertainties were calculated from the uncertainty on the calculation of the mean (max − min/2). The result was calculated as,

$$T_{\text{rec, 1}} = 279.576 \pm 607.941 \text{ K.} \tag{7}$$

Note that it appears that the uncertainty was most likely overestimated. This could have been a result from the calculation of the uncertainty of the mean which might require a more sophisticated uncertainty calculation such as using, uncertainty $= t \cdot s/\sqrt{N}$, where s is the standard deviation, t is the student t-factor and N is the number of data points [25].

The value for $T_{\text{rec, 2}}$ was then calculated graphically by using the hot-cold calibration curve. This curve (shown in Fig. 11) was created by plotting a point for the mean hot temperature and a point for the mean cold temperature and fitting a straight line of the form ($y = mx + b$). Using the python package `Numpy.polyfit` [9] the slope was determined as being $4676.32 \pm 108.5$ K/mW and the y-intercept was determined as $-283.75 \pm 0.023$ K. The absolute value of the y-intercept was then taken as the receiver temperature, and therefore,

$$T_{\text{rec, 2}} = 283.75 \pm 0.023 \text{ K}. \tag{8}$$

When comparing both values, one can see that they are relatively close and therefore any difference was most likely due to imprecision in the calculations or recording of the data. The second method has a much lower uncertainty which shows that is can probably be trusted more than the first value. However, while the calculation method yielded a result with a likely overestimated uncertainty, it is possible that the graphical method yielded an underestimated uncertainty as the uncertainty is very low. Further study on the viability of these uncertainties could be conducted in order to further improve results.

### 3.2.2 Exercise 1.6

Now that the hot-cold calibration had taken place, we were then ready to determine the noise temperature of an unknown source. To do this, the resistor was replaced by the noise diode and the measurements were once again recorded using the PC and 3 recordings of 30 seconds each were taken. The LO was set to 1.450 GHz and a constant amplitude of 0 dBm was set. The calibration was then used to determine

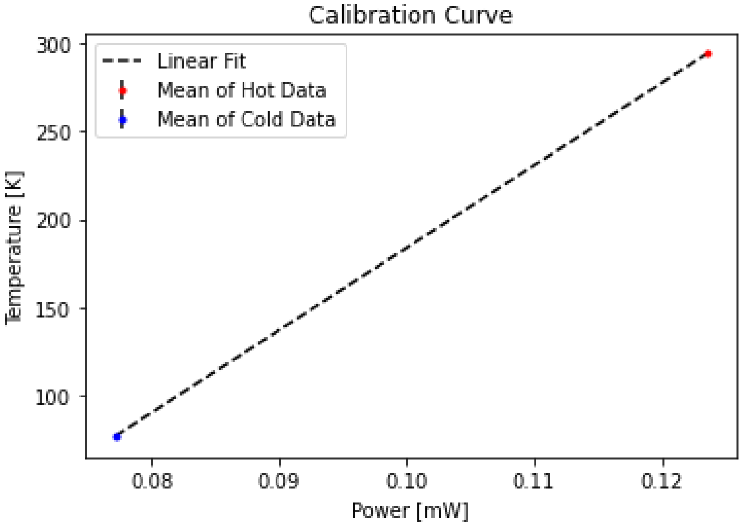

Figure 11: Hot-cold calibration curve. The mean of the hot data has a value of $293 \pm 0.2$ K at a power of $0.123 \pm 0.064$ mW, and the cold data has a value of $77 \pm 1$ K at a power of $0.077 \pm 0.040$ mW. Uncertainties on all points are present, however they are too small to be visible.

the noise temperature.
To do this, the equation of the for $y = mx + b$ was used, where the values of $m$ and $b$ were determined during the calibration, and the value of $x$ used was the mean value of all three noise measurements which was calculated to be $x = -1.876 \pm 0.015$ dBm (shown in Fig. 12). However, once this value was plugged into the calibration equation, the resulting value was of, $y = -9061.026 \pm 215.386$ K, and therefore after taking the absolute value the result was $T = -9061.026 \pm 215.386$ K.

As one may note, the obtained value to $T$ is extremely high compared to the room temperature. This result was most likely just an artifact from the noise diode because since it is not a blackbody, the value of $T$ will not represent it's actual temperature. Since the diode is just producing noise, it could be producing values which lead to a determination of a much higher than a room temperature value. In such a

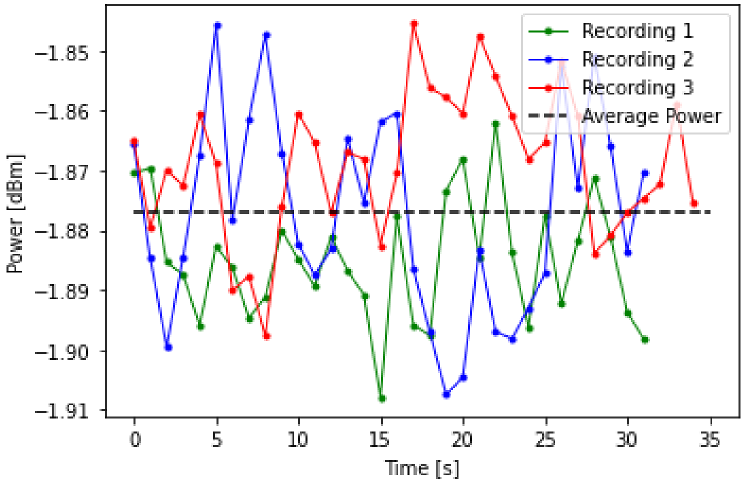

Figure 12: Power vs. time for all three recordings. The mean power of all three recordings is shown in black and was calculated as being $-1.876 \pm 0.015$. Unfortunately no uncertainties were provided by the recording software and therefore no uncertainties are present in this graph. Uncertainties could have been estimated however as they are in reality most likely extremely small, any guessed uncertainty would have been overestimated and would not be accurate. Also note that the lines connecting each of the points are not physical values but are present to help visualize a particular recording's trend.

scenario, a high value of $T$ such as the one determined could even be expected. A possible source of error however was that the calibration of the instruments was not completely accurate. Any small error in calibration could result in a value which is quite wrong.

### 3.2.3 Exercise 1.7

The next task was to simulate atmospheric attenuation. To do this, the variable attenuators were connected in series and inserted between the noise diode and the receiver. The output power was then measured as a function of the variable attenuation from 0 dB to 30 dB in steps of 3. Once the attenuation was changes, it was important to wait for the power level to be stable as there was a short delay between when the attenuation was set and when it appeared on the screen. For each recording, an integration time of 5 seconds was used. As in previous steps, the results were recorded by the PC after which the `hotcold-power.py` program was run and the results were calibrated and then plotted as seen in Fig. 13.

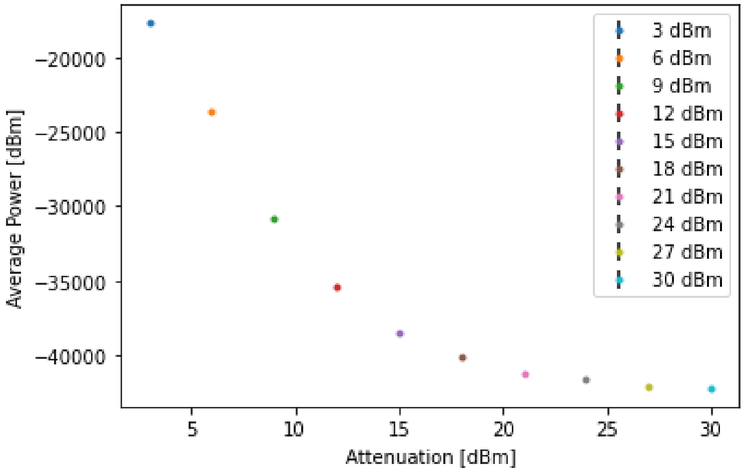

Figure 13: Average power versus the attenuation. Notice the decreasing trend in power as attenuation is increased. Uncertainties on all points are present, however some are too small to be visible.

The results of this task were able to be described by the radiation transport equations,

$$T_{\mathrm{A}} = T_{\mathrm{sys}} - T_{\mathrm{rec}} = \frac{1}{L}T_{\mathrm{b}} + \left(1 - \frac{1}{L}\right)T_{\mathrm{atm}} \tag{9}$$

$$T_{\mathrm{A}} = e^{-\tau}T_{\mathrm{b}} + \left(1 - e^{-\tau}\right)T_{\mathrm{atm}} \tag{10}$$

Where $L$ is the attenuation, therefore $\frac{1}{L}$ is the transmission. $T_{\mathrm{b}}$ is the brightness temperature and $T_{\mathrm{atm}}$ is the atmospheric temperature. Eqn. 10 is specifically the solution to the transport equation for a homogeneous absorber at constant temperature $T_{\mathrm{atm}}$, where $\tau$ is the optical depth [24]. This means that as long at $T_{\mathrm{A}}$ and $T_{\mathrm{atm}}$ are known, it is possible to calculate the transmission and determine the true intensity of a source.

One may see that in Fig. 13, the average power decreases with an increase in attenuation. One may even notice a decreasing trend which resembles the $e^{-\tau}$ behaviour expected from Eqn. 10. It is important to remark however that the average power is extremely low. Even though we are not measuring a blackbody and therefore do not expect the temperatures to be the real temperatures, such extremely high values could potentially be of concern. This once again points to a problem in the calibration process where the calibration of the instruments might not have been accurate enough and could be affecting the results. When the calibration is not applied, the average power ranges between -4 dBm and -9 dBm, which appear to be more reasonable however the calibration step is important to the scientific process and therefore is was applied even if there are chances that it could be wrong. In case there is a problem with the calibration, the same Fig. as Fig. 13 except with uncalibrated values is shown in the appendix as Fig. 27. This calibration should be investigated in order to improve the results.

### 3.2.4 Exercise 1.8

After the attenuation measurement, the next tasks aimed to introduce the students to radio spectroscopy. To do this, a spectrum analyzer was used as a spectroscopic backend and the noise diode and variable attenuators from the previous exercise were replaced by an antenna. This spectrum analyzer allows the bandpass of the receiver to be displayed along with some “emission lines” which are man-made [24]. Man made emission lines such as those which could be seen outside the bandpass can by quite disturbing during astronomical measurement where they would typically be masked if possible.

For this exercise the LO was set to a frequency of 1.45 GHz (CW-mode) and a power of -10 dBm. The signal generator was then set to 1.6 GHz at a power of 0 dBm, the mixer then mixes the two frequencies and an IF frequency was detected at 150 MHz

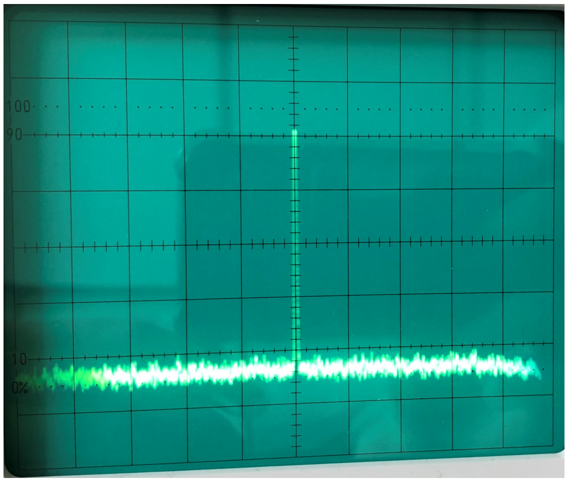

Figure 14: Frequency analyser response. The x-axis is the frequency and the y-axis is the signal amplitude. Signal of the produced "emission line" detected at 150 MHz.

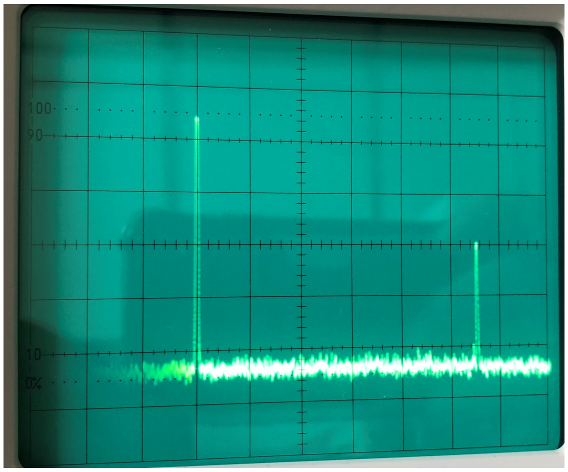

Figure 15: Frequency analyser response showing the produced "emission line" detected at 150 MHz and a harmonic at a higher frequency. Axis are the same as Fig. 14

(Fig. 14). This frequency was also easily determined theoretically,

$$f_{\mathrm{LO}} - f_{\mathrm{RF}} = 1.6\ \mathrm{GHz} - 1.45\ \mathrm{GHz} = 0.150\ \mathrm{GHz} = 150\ \mathrm{MHz}. \tag{11}$$

If the central frequency of the LO was shifted, one could then make out another peak in the spectrum (shown in Fig. 15). This second peak was a harmonic which was present due to imperfections in the mixer. Several other similar peaks should exist periodically at further frequencies on both sides of the main signal, however their amplitudes will be damped compared to the main "emission line".

### 3.2.5 Exercise 1.9

The second radio spectroscopy exercise requires the receiver output to be connected to the SDRplay receiver. The signal was then recorded using different recording length times. Specifically, integration times of 5 s, 15 s, 30 s, 45s, 60s, 75s, 90s, 110s, 120s, and 150s were taken with an uncertainty of ±1 s on all to account for human error when stopping the integration. The same LO and signal generator settings were used as in Exercise 1.8. The average power (noise) was then plotted for each recording time and is displayed in Fig. 16. A linear fit, of the form $y = mx + b$ was then applied to the data points, which had a slope of $m = -0.003 \pm 0.020$ dBm/s and a y-intercept of $b = -2.502 \pm 1.629$ dBm.

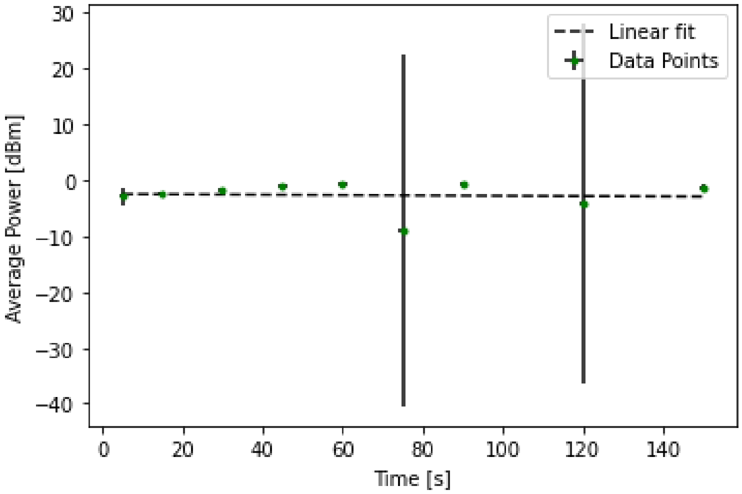

Figure 16: Average power for each recorded time. Notice the small decreasing trend in power as recording time is increased. Uncertainties on all points are present, however some are too small to be visible.

Looking at Fig. 16, from the slope of the linear fit there appears to be an extremely small negative trend the average power as the recording time is increased. This however is contrary to what would be expected as seen from Eqn 12, where the signal should increase, therefore the noise should decrease with longer integration times, $\tau$ [10].

$$\mathrm{SNR} = \frac{T_{\mathrm{A}}}{T_{\mathrm{Sys}}} \left(\Delta\nu \cdot \tau\right)^{1/2} \tag{12}$$

This means that the slope of the linear fit in Fig. 16 should have been increasing and in our case it was not. In general however, the recorded values did not show a very significant trend since the value of the slope was so small, and this could

therefore identify that perhaps the measurements made were not precise enough to measure the expected behaviour. The measurement of bad data would explain the unexpected behaviour and the fact that the trend was not significant.
The room mean square (RMS) values were then calculated for each value using the equation,

$$\Delta T = \frac{T_{\text{Sys}}}{\sqrt{\Delta\nu \cdot \tau}}, \tag{13}$$

which was given in the lab manual [24]. Where $\Delta T$ is the RMS value, $T_{\text{Sys}}$ is the system temperature which was previously calibrated and determined to be $283.75 \pm 0.023$ K, $\Delta\nu$ is the bandwidth and $\tau$ is the integration time. In order to use this equation, a bandwidth of the known frequencies was needed, however no bandwidth was recorded in previous steps and therefore a value had to be estimated. Such a value could have perhaps been estimated if more information was given, for example by using Eqn. 14 if we had been given the number of samples $N$ [10], or Eqn. 15 if the resonant frequency $\nu_c$ had been calculated and the quality factor $Q$ was determined [15].

$$\Delta\nu = \frac{1}{2}\frac{N}{\tau} \tag{14}$$

$$\Delta\nu = \frac{\nu_c}{Q} \tag{15}$$

Unfortunately since the values for the above equation were not provided or determined, it was therefore decided that at a frequency of 150 MHz, it was reasonable to estimate a bandwidth of $\Delta\nu = 1 \pm 0.5$ MHz. This value was then converted to Hz in Eqn. 13 and the radiometer equation was then used to plot the RMS noise versus the recorded time (shown in Fig. 17). A linear fit, of the form $y = mx + b$ was then applied to the data points, which had a slope of $m = -0.001 \pm 0.0002$ K/s and a y-intercept of $b = 0.084 \pm 0.013$ K.

From Fig. 17, the linear fit demonstrates a decrease in the RMS noise as the recording time was increased. This trend was expected since in Eqn. 13, the integration time $\tau$ is in the denominator, and therefore one would expect that as the integration time increased, the RMS noise should decrease.

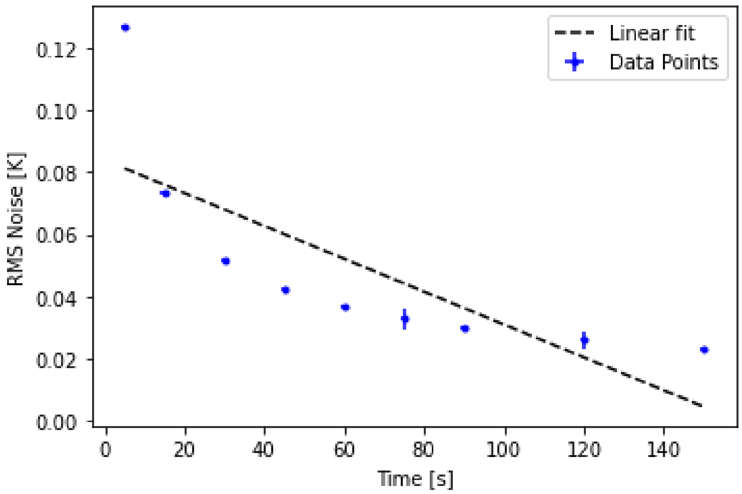

Figure 17: RMS noise for each recorded time. Notice the decreasing trend in power as recording time is increased. Uncertainties on all points are present, however some are too small to be visible.

The next step for this section was to calculate the integrated line flux. This was done after running the `hotcold-power.py` program on each measurement and the `line-detect.py` code was run for 15s and 30s. For a more comprehensive analysis, this last script could have been run on all measurements of different times, however due to time restrictions the tutors instructed to only use the measurements of 15s (Fig. 18) and 30s (Fig. 19).

The integrated line flux was then calculated for both recording by calculating the area under the signal. This was done using two different methods with the `Python` packages `Scipy.integrate.simps` and `Scipy.integrate.trapz` [11]. The two separate methods were used as a way to compare different integration methods and see if our final results were consistent. Performing the integral of an intensity will yield the net power radiated, $P_{\text{net}}$ [17], therefore the integrated line flux is equivalent to $P_{\text{net}}$ and therefore our resulting values will have units of Watts. For the 15 second measurement, the `Scipy.integrate.simps` method yielded a value of $P_{\text{net, 15}} = 0.204$ W, whereas the `Scipy.integrate.trapz` method yielded a value of $P_{\text{net, 15}} = 0.200$

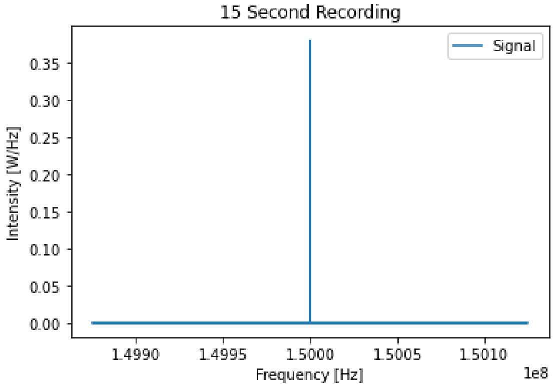

Figure 18: Frequency spectrum for the signal recorded during 15 seconds.

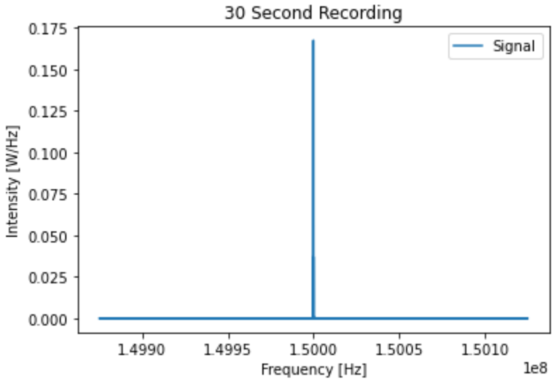

Figure 19: Frequency spectrum for the signal recorded during 30 seconds.

W. For the 30 second measurement, the `Scipy.integrate.simps` method yielded a value of $P_{\text{net, }30} = 0.231$ W, whereas the `Scipy.integrate.trapz` method yielded a value of $P_{\text{net, }30} = 0.225$ W. In both cases these values were very close to each other and therefore the integral was most likely correctly calculated in both methods. For both integration methods, a linear fit was applied to examine the behaviour of the integrated line flux, and are present in the Appendix as Fig 28 and Fig. 29. In both the integration methods, a positive linear trend is noticed however since there are unfortunately since there are only two data points, this trend carries no statistical significance.
Unfortunately no uncertainty was provided by the recording software, in future work it would be important to calculate an uncertainty on both values. It would be especially important in a situation such as this one, as both integration methods probably produce results which lie within the other's uncertainty but unfortunately this cannot be known for certain in this report. In future reports, it would also be important to take measurements of more recording times, such as in the previous part, in order to further analyze the trend of the integrated line flux as time is increased.

The last step of this section was to estimate the temperature of the source, assuming that the line comes from a cloud in thermal equilibrium. In such a situation, where

$h\nu << kT$ we were able to use the Rayleigh–Jeans law to calculate the temperature of that source according to Eqn. 16.

$$T_\mathrm{b} = \frac{I_\nu c^2}{2k_\mathrm{B}\nu^2} \tag{16}$$

Where $I_\nu$ is the intensity of the line in Hz, $c$ is the speed of light, $k_\mathrm{B} = 1.380649 \cdot 10^{-23}$ $\mathrm{m^2{\cdot}kg{\cdot}s^{-2}{\cdot}K^{-1}}$ is the Boltzmann constant and $\nu$ is the frequency. In both the recordings, the frequency peak was of $\nu = 150$ MHz. For the 15 second recording, $I_\nu = 0.380$ W/m$^2$, and for the 30 second recording, $I_\nu = 0.167$ W/m$^2$. Plugging the values into the equation results in a value for the 15 second recording as $T_{\mathrm{b},\,15} = 5.492 \cdot 10^{22}$ K and a value for the 30 second recording of $T_\mathrm{b} = 2.421 \cdot 10^{22}$ K.

Here it is important to note that these brightness temperature values are extremely high. This is because the values are not physical temperatures because the brightness temperature equation only gives the actual physical temperature of an object when they can be considered as a blackbody. As our experiment is not even actually observing a physical object, it is certainly not a blackbody.

Once again it is important to consider here that no uncertainty values were provided with the data and therefore the resulting values do not contain any uncertainties. For a properly thorough report, it would be important to provide uncertainties on all measurements and results.

### 3.2.6 Exercise 1.10

In this final exercise, the goal was to determine the possible frequencies of the LO when observing at 1.8 GHz and to test the setup of the signal generator. The second task was determining the emitting frequency of a mobile phone. This exercise however had to be conducted theoretically rather than practically as the tutor suspected that this exercise might be causing problems with the superheterodyne receiver and causing it to break.

In order to observe a specific frequency we re-arrange Eqn. 11 to get,

$$\begin{aligned} f_{\mathrm{IF}} &= f_{\mathrm{LO}} - f_{\mathrm{RF}} \\ f_{\mathrm{LO}} &= f_{\mathrm{RF}} \pm f_{\mathrm{IF}}, \end{aligned} \tag{17}$$

Since we have $f_{\mathrm{IF}} = 150$ MHz,

$$f_{\mathrm{LO}} = 1800\mathrm{MHz} \pm 150\mathrm{MHz}, \tag{18}$$

So in order to observe the frequency of 1.8 GHz, the LO should be set to 1.65 GHz or 1.95 GHz.

The emitting frequency of a mobile phone could then be theoretically calculated. Practically, this would have been done by starting a phone call and pointing the phone towards the antenna. The signal would then be seen on the frequency analyzer. Once could then detect an uplink frequency and a downlink frequency on the LO, after which one could add 150 MHz to find the actual frequency of the phone. If this exercise were to have been performed practically and correctly, one would expect to have a resulting frequency value either between 800-900 MHz or between 1800-1950 MHz depending on the type of phone that was used [4].

## 4 Setting Up a Twin Radio Interferometer

In this part of the experiment, a twin radio interferometer is used to record radio emission from the Sun and produce a radio image of the Sun. The interferometer consists of two identical radio dishes 90cm in diameter connected together through a correlator. The signals coming from the individual dished are correlated in the correlator whose task is to multiply the two signals also known as 'cross-correlation' to give a interference/fringe pattern with the fringe width being comparable to the angular resolution of the system which depends on the separation between the two dishes. However, we were not able to perform this task due to bad weather conditions and hence, had to use data from the previous experiment. All bits of data analysis performed in this section is based upon the data received from the previous experiment.

The antennas record the raw data in the form of power received as a function of time. This data is very noisy and a noise reduction algorithm needs to be applied to get a RFI mitigated signal. This is done by using the python script given in the manual and the raw data plots for the two methods for Antenna A can be found in the Appendix 6

## 4.1 Still Scan

In this observation, the antenna are kept at a fixed position and the Sun is allowed to pass through the field of view of the telescope system. A schematic view of how this is done can be seen in 20.

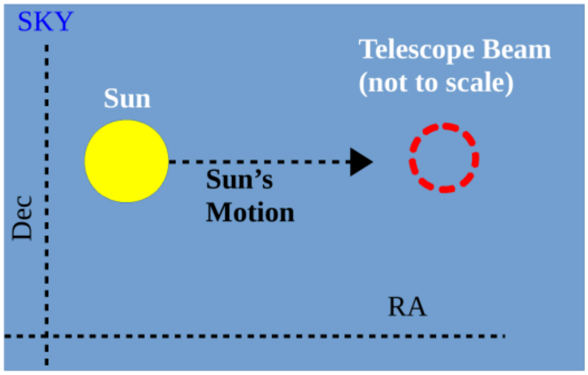

Figure 20: Schematic View of the Still Scan Method (credits:[24])

The raw data from the still scan was passed through the given python script to perform a noise reduction and certain cutoffs in the time domain were applied to the dataset such that we only record the signals when the Sun just passes over the antenna system. The intensity vs time plots generated after following these steps for data from both antennae can be seen in Fig. 21.

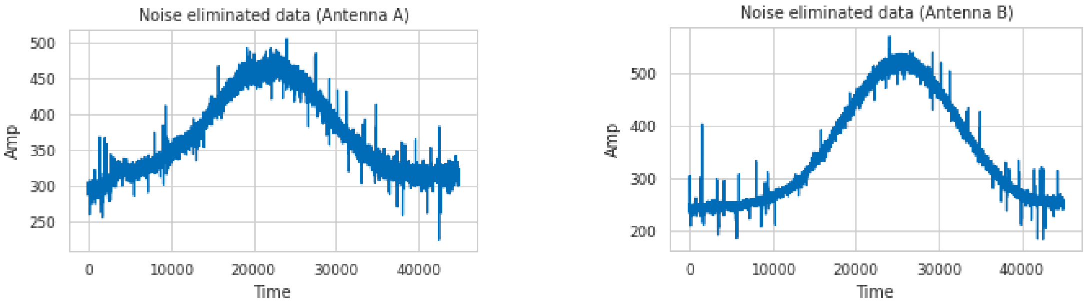

(a) Noise reduced data from Antenna A

(b) Noise reduced data from Antenna B

Figure 21: Noise Reduced data from the Still Scan Method

## 4.2 Declination Scan

In this method, the RA of the telescopes was fixed while their declination was changed such that the interferometer scanned the entire Sun thus able to produce an image. The visualization of this can be seen in the schematic diagram shown in Fig. 22.

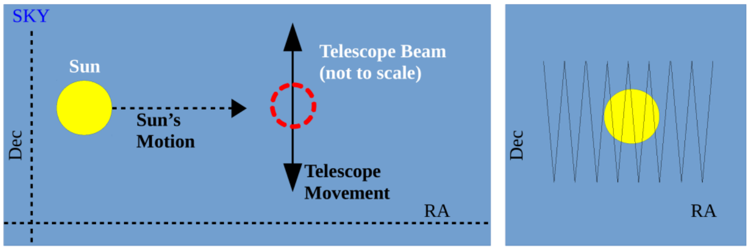

Figure 22: Schematic View of the Declination Scan Method (credits:[24])

It can be verified that the procedure was performed correctly by plotting the telescope Declination as a function of the Right Ascension. This is shown in Fig. 23

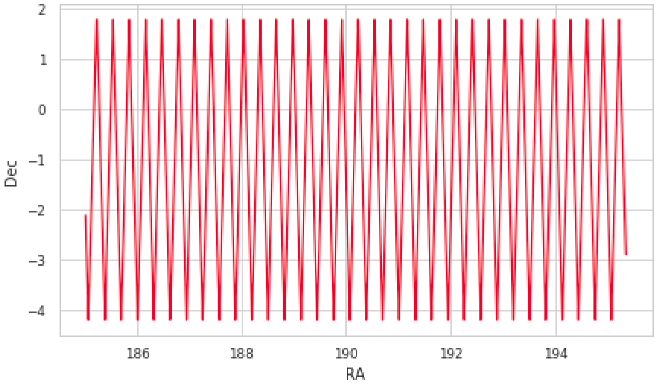

Figure 23: RA and Dec plot of the telescope

After recording the declination scan data, a similar noise reduction technique was applied to it as that for the Still Scan and the noise reduced dynamic plots were produced for both the antennas. These can be seen in Fig. 24. One thing to notice in these plots is the regularly spaced peaks unlike the still scan since the telescope declination was being changed during the observation. Thus, we expect these dynamic plots to precisely follow the telescope movement.

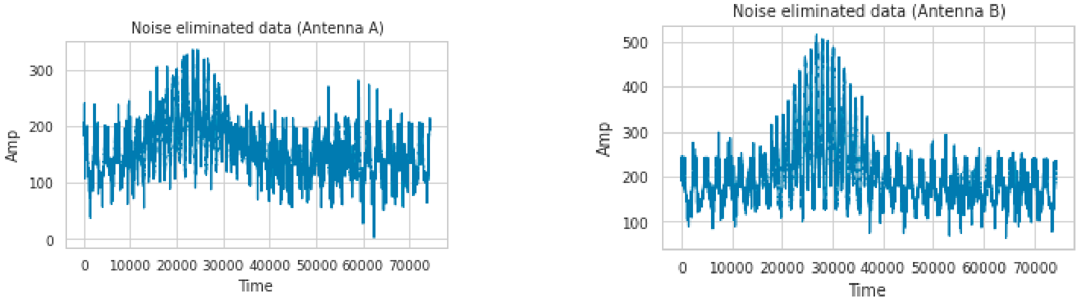

(a) Noise reduced data from Antenna A

(b) Noise reduced data from Antenna B

Figure 24: Noise Reduced data from the Declination Scan Method

After eliminating most of the noise from the observation, the last section of the provided python script was used to produce an Image of the Sun. This code produces three images, two images from the individual antenna and a final interferometric image from the interferometer. These results can be seen in Figs. 25 and 26

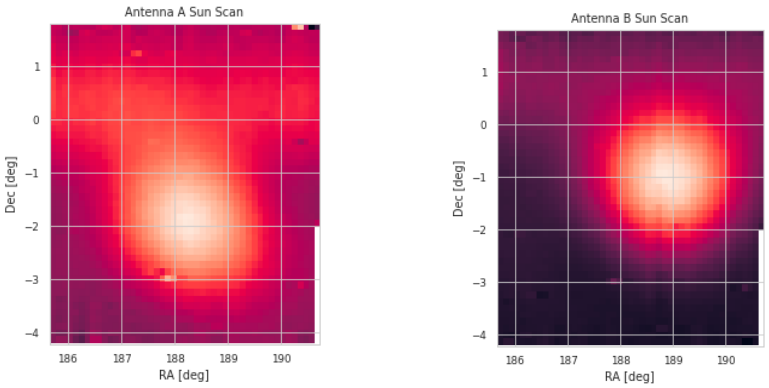

(a) Image created from Antenna A

(b) Image created from Antenna B

Figure 25: Images of the Radio Sun from the two individual Radio Dishes

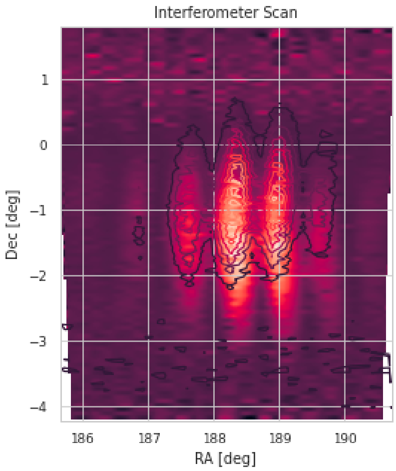

Figure 26: Radio Sun as imaged by the interferometer

It can be seen in the above images that the results produced from the individual antennas have a poor angular resolution. Moreover, the image produced by Antenna A is all over the place which shows that the observing run was not carried out very precisely for that antenna. However, when me correlate the data from the two dishes, we get interferometric fringes and it can be seen from the interferometric images that this gives a much higher resolution. If the baseline between the antennas were to be increased, it would give more number of interferometric fringes with smaller spacings and hence a more better image resolution.

From these observations, we can try to find the angular extent of the Sun. In this part, we used the interferometric image of the Sun and found out its angular diameter to be roughly $\sim 1.8°$. In the optical regime, the angular diameter of the Sun is about 0.53° [14]. This is the extent of the solar photosphere. However, from our results, it can be seen that the radio Sun is almost three times bigger than the Sun. This is because the radio emission from the Sun extends up to the solar corona. Our instrument is tuned to observe the Sun in the **X-band** (8-12 GHz). Hence, the radio extent of the Sun we see is purely due to the thermal emission acting as a black body [12].

From the angular diameter, the actual extent of the Sun can be calculated using the following relation:

$$\theta = \frac{Diameter\ of\ the\ Sun}{Distance\ between\ the\ Sun\ and\ Earth} \tag{19}$$

In this formula, the current average distance to the Sun was assumed to be 148.03 million kilometers [reference]. From this equation, the diameter of the Sun was found out to be $D_{sun} = 266.45 \times 10^9 m$. This is the diameter of the radio Sun and varies as a function of frequency and solar activity [2].

# 5 Conclusion

## 5.1 Part I: Setting Up a Radio-Astronomical Receiver

### 5.1.1 Components of a Superheterodyne Receiver

The first tasks of this lab were to study all of the different components of the superheterodyne receiver. The gain of two amplifiers (high power and low power) were measured by fitting a straight line to their linear response. A high power filter as well as a low power filter were then studied by determining their bandwidths along with their maximum output power, insertion loss and adjacent-band rejections. The mixer was then studied to verify that its output power depended linearly on the RF signal and a conversion loss was calculated.

### 5.1.2 Components of a Superheterodyne Receiver

In this step of the lab, the simplified setup was replaced by an actual superheterodyne receiver. Here a hot-cold calibration was first performed and a system temperature temperature was determined using two separate methods. From this information, the noise diode temperature was measured and finally atmospheric attenuation was simulated by connecting two attenuators in series.

### 5.1.3 Radio Spectroscopy

The first radio spectroscopy exercise was to study the output of the receiver using a frequency analyser. The part involved using an SDR to study the response of the receiver, where average power and rms values were investigated according to different integration times.

### 5.1.4 Further Discussion

All uncertainties were calculated according to Gaussian error propagation given in Eq. 20 and Eq. 21. It is important to note however that there were many flaws with how the uncertanties were calculated in this report, the most important of which were that many of the results produced by the instruments did not produce uncertainties and therefore most of the uncertainty values had to be guessed to the best of our knowledge. In further work it would be important to take a deeper look at the uncertainties and create a reasonable estimate for all values in this report.
There were also many parts of this lab which were either not functioning or had serious imprecision. In order to improve the lab, it would be important to acquire better instruments which can work to a higher precision.

## 5.2 Part II: Twin Radio Interferometer

In this part, raw data was obtained from interferometric observation of the Sun in the X-Band. The analysis done in this part is limited by the raw data which was provided by the tutors since bad weather conditions did not allow to take any real time observations. Moreover, the provided raw data was first cleaned by using a noise reduction script provided by the tutors. Then, the two different scans were used for different analysis purposes. The still scan gave a plot where data cuts were given to constrain the time when the Sun enters the telescope field of view and exits it giving smooth rise and fall in the flux levels as the observations proceed. In the declination scan, an image of the Sun was produced for the noise reduced data. The image from individual antennas and the interferometric image were produced in this analysis. From the images we see, we conclude that the performance of Antenna A was not optimum during the course of the observations. Possible reasons can be inaccurate tracking or some defects in the receiver backend for the antenna. The interferometric image gives a better resolution which allowed us to constrain the solar diameter to 266.45 million kilometers. As a comparison, it is not possible to find a fixed value for this diameter in the literature as the radio Sun has a high variability and the size also varies as a function of the observing frequency. However, the calculated diameter does conclude that the diameter of the radio Sun is larger than in the optical regime.

# References

[1] Valvo(1999): *Insertion loss measurement.*

[2] T.K. Das, H. Sarkar A.K. Sen(1999): *The Ratio of the radio and optical diameters of the sun at centimeter wavelengths.*

[3] Hunter, J. D.(2007): *Matplotlib: A 2D graphics environment*, 3: 90–95.

[4] Army, U.S.(2009): *U.S. Army Public Health Command.*

[5] Canada, Natural Resources(2015): *Spectral Resolution.*

[6] Mini Circuits(2015): *Understanding mixers – terms defined, and measuring performance.*

[7] Arar, Steve(2018): *Basics of digital down-conversion in DSP - technical articles.*

[8] Team, Editorial(2018): *What is Conversion Loss.*

[9] Harris, Charles R. u.a.(2020): *Array programming with NumPy*, 7825: 357–362.

[10] Woan, G.(2020): *The radiometer equation – a more careful look.*

[11] Virtanen, Pauli u.a.(2020): *SciPy 1.0: Fundamental Algorithms for Scientific Computing in Python*261–272.

[12] PhysicsOpenLab(2020): *Solar Radio Emission.*

[13] Astrophysics(2021): *back end instrument.*

[14] Wikipedia(2022): *Angular diameter — Wikipedia, The Free Encyclopedia.*

[15] Team, Calculator Academy(2022): *Bandwidth calculator.*

[16] EverythingRF(2022): *Insertion Loss.*

[17] Wikipedia(2022): *Intensity (physics).*

[18] Wikipedia(2022): *Solar radio emission — Wikipedia, The Free Encyclopedia.*

[19] Giuliano Muratore, Davide Micheli(2022): *Solar radio emission as a disturbance of radiomobile networks.*

[20] Bole, Dineley W. O. (1990): *Radar and ARPA manual.* , Heinemann Newnes.

[21] Csete, Alexandru (2021): *Gqrx SDR*
.

[22] Hewes, John (2006): *AC, DC and electrical signals.* , The Electronics Club.

[23] Kuphaldt, T.R. (2011): *Lessons in Electric Circuits: An Encyclopedic Text & Reference Guide (6 Volumes Set).* , Koros Press Limited.

[24] Lab, Tutors (2020): *Radio Astronomy Lab.* , The Argelander-Institut für Astronomie.

[25] Moore, Thomas A (2017): *The Uncertainty of the Mean.* , McGraw Hill.

[26] Notes, Electronics (No Date): *Adjacent channel selectivity*
.

[27] Van Rossum, Guido / Drake Jr, Fred L (1995): *Python reference manual.* , Centrum voor Wiskunde en Informatica Amsterdam.

# 6 Appendix

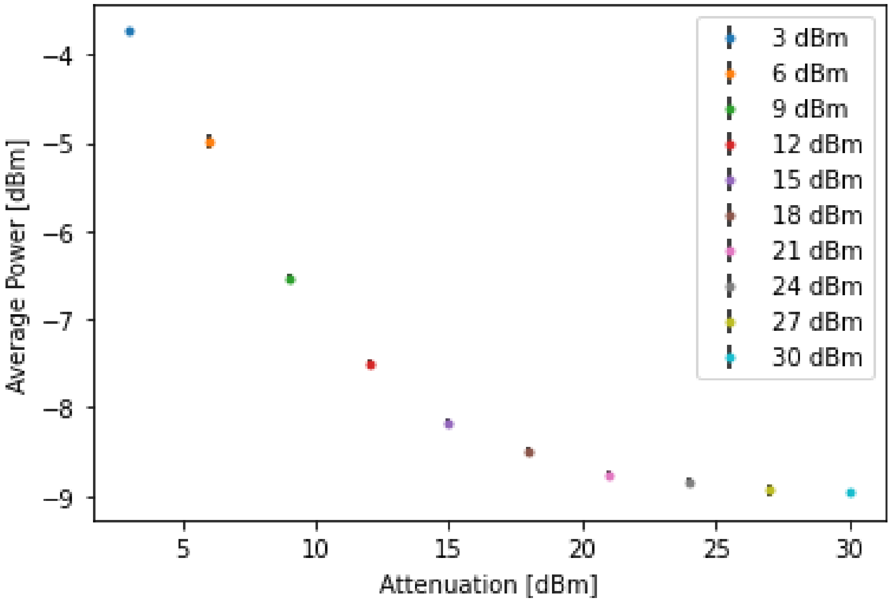

Figure 27: Uncalibrated average power versus the attenuation. Notice the decreasing trend in power as attenuation is increased. Uncertainties on all points are present, however some are too small to be visible.

The error propagation for an addition or subtraction is given by,

$$\delta Q = \sqrt{(\delta a)^2 + (\delta b)^2 + \cdots + (\delta c)^2 + (\delta x)^2 + (\delta y)^2 + \cdots + (\delta z)^2}. \tag{20}$$

Standard Gaussian error propagation is given by the general form of Summation in Quadrature,

$$\delta f\,(x, y, ...) = \sqrt{\left(\frac{\partial f}{\partial x}\delta x\right)^2 + \left(\frac{\partial f}{\partial y}\delta y\right)^2 + \cdots} \tag{21}$$

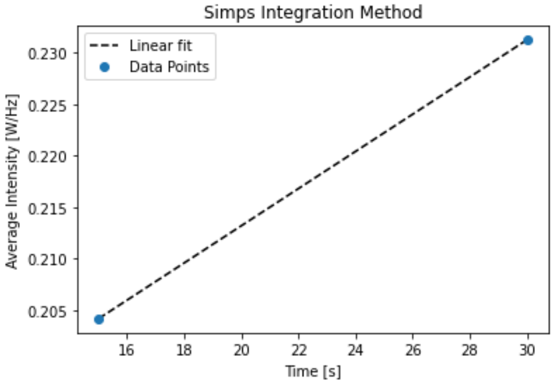

Figure 28: Linear fit of the form $y = mx + b$ to examine the behaviour of the integrated line flux using the Simps integration method. Slope was of m=0.002 and y-intercept was of b=0.177.

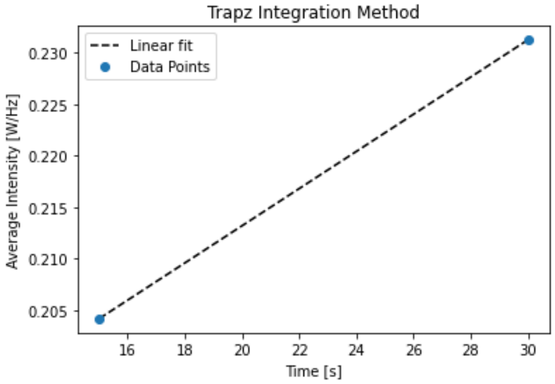

Figure 29: Linear fit of the form $y = mx + b$ to examine the behaviour of the integrated line flux using the Trapz integration method, Slope was of m=0.002 and y-intercept was of b=0.173.

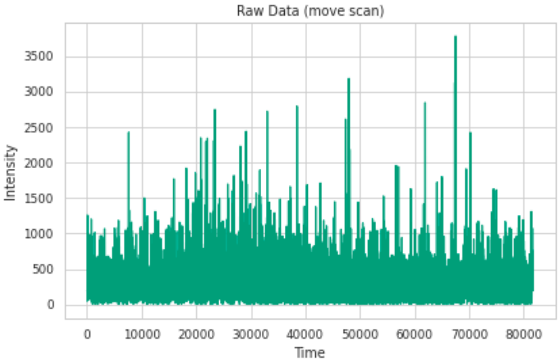

Figure 30: Raw Data from Declination Scan for Antenna A

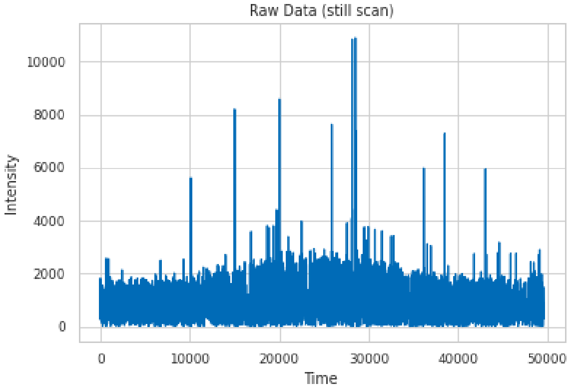

Figure 31: Raw Data from Still Scan for Antenna A